

# Machine learning force fields: Construction, validation, and outlook

V. Botu,<sup>\*,†</sup> R. Batra,<sup>‡</sup> J. Chapman,<sup>¶</sup> and R. Ramprasad<sup>‡</sup>

*Department of Chemical & Biomolecular Engineering, University of Connecticut, Storrs, CT,*

*Department of Materials Science & Engineering, University of Connecticut, Storrs, CT, and*

*Department of Materials Science, University of Connecticut, Storrs, CT*

E-mail: botuvenkatesh@gmail.com

## Abstract

Force fields developed with machine learning methods in tandem with quantum mechanics are beginning to find merit, given their (i) low cost, (ii) accuracy, and (iii) versatility. Recently, we proposed a force based approach, wherein, the vectorial force on an atom is computed directly from its environment. Here, we discuss a multi-step workflow for their construction, which begins with generating diverse reference atomic environment and force data, choosing a representation for the atomic environments, down selecting a representative set, and lastly the learning method itself, for the case of AI. Further, methods to judge force prediction accuracy are proposed allowing for an adaptive refinement of the force field. The constructed force field is then validated by simulating complex materials phenomena such as melting and stress-strain behavior, which truly go beyond the realm of *ab initio* methods both in length and time scales.

---

\*To whom correspondence should be addressed

<sup>†</sup>Department of Chemical & Biomolecular Engineering, University of Connecticut, Storrs, CT

<sup>‡</sup>Department of Materials Science & Engineering, University of Connecticut, Storrs, CT

<sup>¶</sup>Department of Materials Science, University of Connecticut, Storrs, CT

## Introduction

Materials modeling approaches largely fall in two broad categories: one based on quantum mechanical methods (e.g., density functional theory), and the other based on semi-empirical analytical interatomic potentials or force fields (e.g., Stillinger-Weber potentials, embedded atom method, etc.)<sup>1-9</sup> Choosing between the two approaches depends on which side of the cost-accuracy trade-off one wishes to be at. Quantum mechanical methods (also referred to as *ab initio* or first principles methods) are versatile, and offer the capability to accurately model a range of chemistries and chemical environments. But such methods remain computationally very demanding. Practical and routine applications of these methods at the present time are limited to studies of phenomena whose typical length and time scales are of the order of nanometers and picoseconds, respectively. Semi-empirical methods capture the essence of these interatomic interactions in a simple manner via parameterized analytical functional forms, and thus offer inexpensive solutions to the materials simulation problem. However, their applicability is severely restricted to the domain of chemistries and chemical environments intended, or considered during parameterization.<sup>10</sup> It is unclear whether the underlying framework allows for a systematic and continuous improvement in the predictive capability of newer environments.

The present contribution pertains to a data-driven approach by which flexible and adaptive force fields may be developed, potentially addressing the challenges posed. By using carefully created benchmark data (say, from quantum mechanics based materials simulations) as the starting point, non-linear associations between atomic configurations and potential energies (or forces, more pertinent to the present contribution) may be learned by induction.<sup>11-13</sup> This data-driven paradigm, popularly referred to as machine learning, has been shown by many groups to lead to viable pathways for the creation of interatomic potentials that; (1) surpass conventional interatomic potentials both in accuracy and versatility, (2) surpass quantum mechanical methods in cost (by orders of magnitude), and (3) rival quantum mechanics in accuracy,<sup>14-16</sup> at least within the configurational and chemical domains encompassed by the benchmark dataset used in the training of the potential.

A new recent development within the topic of machine learning based interatomic potentials

is the realization that the vectorial force experienced by a particular atom may be learned and predicted directly given just a configuration of atoms.<sup>17-19</sup> This capability is particularly appealing as the atomic force is a local quantity purely determined by the local environment, in contrast to the total potential energy which is a global property of the system as a whole. A large body of materials simulations, such as geometry optimization and molecular dynamics simulations, require the atomic force as the sole necessary input ingredient.<sup>1</sup> Note that partitioning the total potential energy into individual atomic contributions, conventionally adopted in semi-empirical interatomic potentials, is a matter of convenience of construction, rather than being a fundamental requirement.

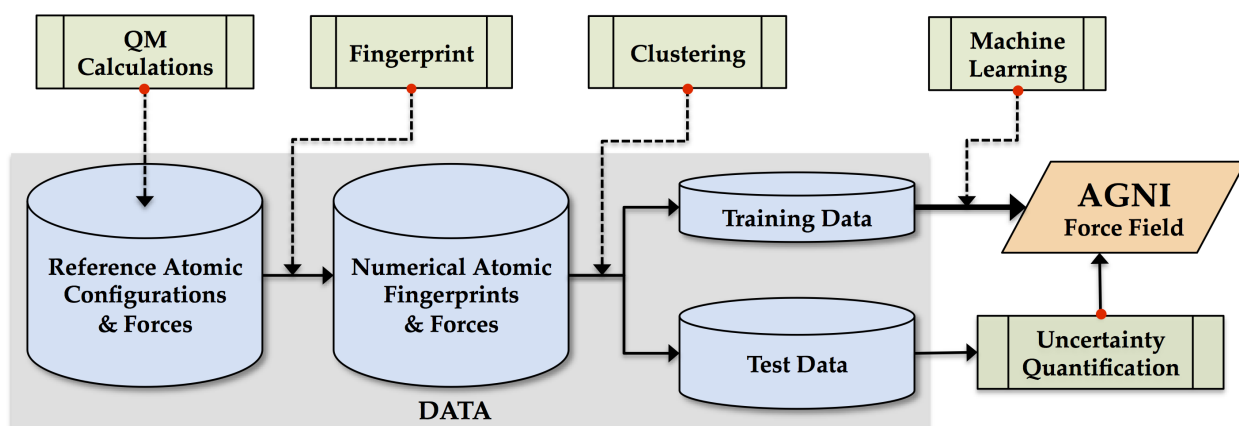


Figure 1: Flowchart illustrating the workflow in constructing AGNI force fields - generating reference atomic configurations and forces with quantum mechanical methods, fingerprinting atomic environments, rational selection of training and test datasets, mapping atomic fingerprints to forces using machine learning methods, and quantifying uncertainty in predictions made.

This article deals specifically with using machine learning methods to create an atomic force prediction capability, i.e., a force field. As recently pointed out, this force field is *Adaptive* (i.e., new configurational environments can be systematically added to improve the versatility of the force field, as required), *Generalizable* (i.e., the scheme can be extended to any collection of elements for which reliable reference calculations can be performed), and is *Neighborhood Informed* (i.e., a numerical fingerprint that represents the atomic environment around the reference atom is mapped to the atomic force with chemical accuracy).<sup>17,18</sup> The force field is henceforth dubbed AGNI.

Here, we start with a detailed description of the key steps involved in constructing an AGNI

force field. These include: (1) creation of a reference dataset derived from a plethora of diverse atomic environments of interest and the corresponding atomic forces computed using a chosen quantum mechanical method; (2) fingerprinting every atomic environment in a manner that will allow the fingerprint to be mapped to atomic force components; (3) choosing a subset of the reference dataset (the “training” set) using clustering techniques to optimize the learning process while insuring that the training set represents the diversity encompassed by the original reference dataset; (4) learning from the training set, thus leading to a non-linear mapping between the training set fingerprints and the forces, followed by testing the learned model on the remainder of the dataset using best-statistical practices; and (5) finally, estimation of the expected levels of uncertainty of each force prediction, so that one may determine when the force field is being used outside its domain of applicability. The entire workflow involved in the creation of the AGNI force field is portrayed schematically in Figure 1. Additional comments pertaining to the last step of the workflow in Figure 1 are in order. Uncertainty quantification is essential to recognize when the force field is operating outside its domain of applicability. Ideally, larger the uncertainty of the force prediction for an atom in a given environment, greater is the likelihood that the environment is “new”. By imposing a threshold and monitoring the uncertainty we may wish to augment the training set with the corresponding new atomic environment(s), and follow the workflow in Figure 1. This helps build force fields that are truly *adaptable*. Initial steps towards quantifying this uncertainty in force predictions are undertaken.

In our previous work, a preliminary version of the AGNI force field for AI was used to demonstrate its capability with respect to predicting structural, transport or vibrational properties of materials.<sup>18</sup> In this work we further extends its scope, by including more diverse atomic environments and its ability to simulate even more complex phenomena - such as surface melting and stress-strain behavior. Furthermore, although AGNI is built to provide atomic forces, we demonstrate that accurate total potential energies can be retrieved either during the course of a molecular dynamics simulation or along a reaction coordinate, through appropriate integration of atomic forces.

The rest of the paper is organized as follows. In the first half of the work we guide the readers

through each step of the force field construction workflow, shown in Figure 1, to develop a general-purpose AI force field. This is then followed by a demonstration of the force field in atomistic simulations to validate the rigor of the construction protocol. We conclude with an outlook on using machine learning force fields in the field of atomistic materials modeling, and the challenges that yet remain to be addressed.

## Generating reference data

The construction of AGNI force fields begins with data. Here, we start by building several periodic and non-periodical equilibrium configurations (consisting of a few atoms, c.f., Figure 2), such as; (i) defect free bulk, (ii) surfaces, (iii) point defects - vacancies and adatoms, (iv) isolated clusters, (v) grain boundaries, (vi) lattice expansion and compression, and (vii) edge type dislocations. These configurations are so chosen to mimic the diverse environments an atom could exist in, and forms a critical first step in constructing generalizable force fields. It is by no means a complete list and one could continuously add non-redundant configurations to it (methods to identify such redundancies are discussed later). The vectorial force components on each atom, in the equilibrium configurations amassed, are then computed by quantum mechanical based density functional theory (DFT) calculations.<sup>20,21</sup> To correctly describe the non-equilibrium behavior of an atom in response to a perturbation (due to thermal vibrations, pressure or other sources), it is equally necessary to construct non-equilibrium atomic environments - to learn the array of forces experienced by an atom. A convenient and quick means to sampling such non-equilibrium environments is with *ab initio* molecular dynamics (MD) simulations.<sup>22</sup> Here, starting with the equilibrium configurations in Figure 2 constant temperature MD simulations were carried out across a range of temperatures between 200 - 800 K, resulting in a diverse set of reference atomic environments and forces (c.f., Table 1) - needed to learn (indirectly) the underlying potential energy surface.

From within the millions of reference atomic environments collected, a subset of them are chosen as training environments to construct the force fields. The particular choice of environments

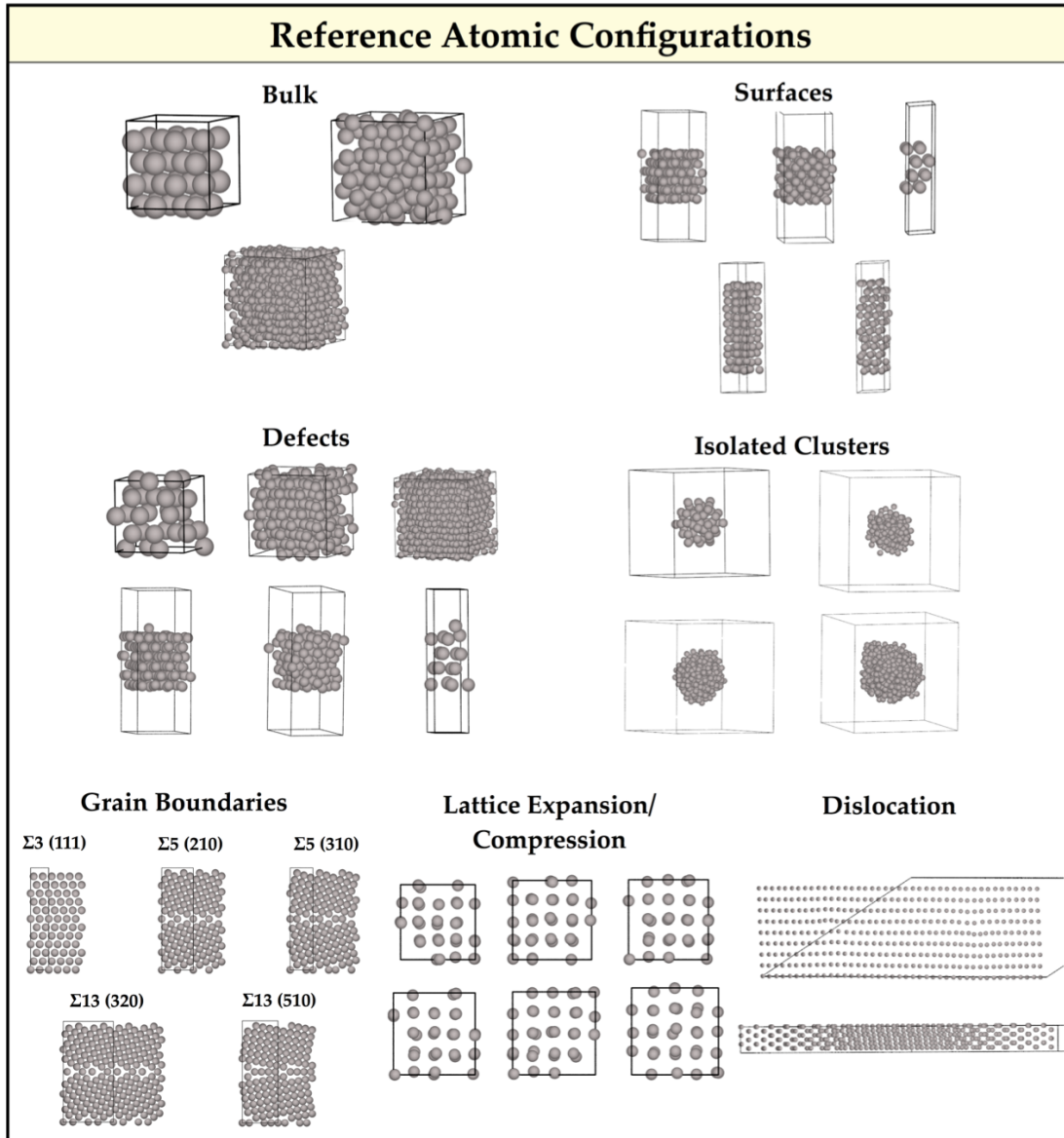


Figure 2: Reference configurations used to sample atomic environments for training and testing of AGNI force fields; (i) bulk, (ii) surfaces, (iii) defects (vacancies and adatoms), (iv) isolated clusters, (v) grain boundaries, (vi) lattice expansion and compression, and (vii) dislocation.

plays a critical role in the generalizability of such data-driven force fields. To better understand such limits imposed by data choices we construct four training datasets, labeled as A, B, C, and D, with increasing complexity and diversity of atomic environments contained (c.f., Table 1). Also a fifth dataset, E, consisting of configurations never used during force field construction are gathered to demonstrate the transferability of AGNI force fields.

Table 1: Atomic environment makeup for the five datasets; A, B, C, D and E. For each dataset we generate a training and test set (except for dataset E, where only a test set is created) - the former used to construct the force field and the later to validate it. The number of new environments added is indicated in the last column.

<b>Dataset</b>	<b>Atomic Envs. from Reference Configurations</b>	<b>Number of Envs.</b>
<b>A</b>	Defect free bulk fcc and bcc.	20385
<b>B</b>	Dataset A + (100), (110), (111), (200), and (333) surfaces.	211255
<b>C</b>	Dataset B + Defects in bulk fcc with 1, 2 and 6 randomly distributed vacancies and adatom on (100), (110) and (111) surfaces.	1502856
<b>D</b>	Dataset C + Isolated clusters of 5Å, 8Å, 10Å, and 12Å. $\Sigma 3$ (111), $\Sigma 5$ (210), $\Sigma 5$ (310), $\Sigma 13$ (320), and $\Sigma 13$ (510) grain boundaries, varying lattice vectors by $\pm 7$ % of equilibrium,	586679
<b>E</b>	edge dislocation along $(11\bar{2})$ direction.	394116

All force and MD calculations were done with VASP, a plane-wave based DFT software.<sup>23,24</sup> The generalized gradient approximation functional parameterized by Perdew, Burke, and Ernzerhof to treat the electronic exchange-correlation interaction, the projector augmented wave potentials, and plane-wave basis functions up to a kinetic energy cutoff of 520 eV were used.<sup>25,26</sup> A  $14 \times 14 \times 14$   $\Gamma$ -centered k-point mesh was used for the primitive Al unit cell, and scaled according to the unit cell size. A timestep of 0.5 fs was chosen for the MD simulations.

# Fingerprinting reference environments

## Functional form

The availability of vectorial force components,  $F^u$ , where  $u \subset (x, y, z)$ , necessitates a numerical representation of the atomic environment that conforms with this directional dependence. Further, it should also remain invariant to basic atomic transformation operations, such as translation, rotation or permutation. One such representation with the necessary prerequisites is given below,

$$V_i^u(\eta) = \sum_{j \neq i} \frac{r_{ij}^u}{r_{ij}} \cdot e^{-\left(\frac{r_{ij}}{\eta}\right)^2} \cdot f_d(r_{ij}). \quad (1)$$

Here,  $r_{ij}$  is the distance between atoms  $i$  and  $j$  ( $\|\mathbf{r}_j - \mathbf{r}_i\|$ ), while  $r_{ij}^u$  is a scalar projection of this distance along a direction  $\hat{u}$  (c.f., Figure 3).  $\eta$  is the Gaussian function width.  $f_d(r_{ij}) = 0.5 \left[ \cos\left(\frac{\pi r_{ij}}{R_c}\right) + 1 \right]$ , is a damping function for atoms within the cutoff distance ( $R_c$ ), and is zero elsewhere. The summation in Eq. ?? runs over all neighboring atoms within an arbitrarily large  $R_c$  (8 Å, in the present work).

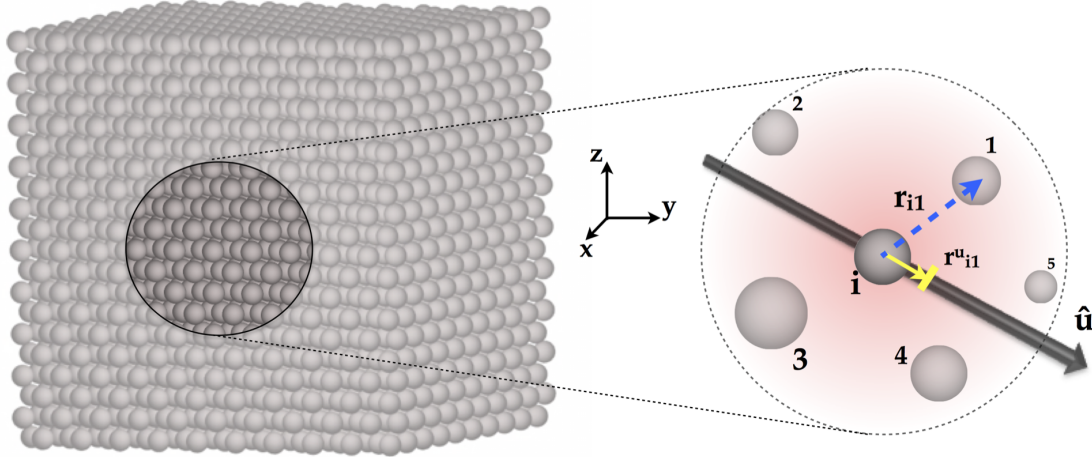


Figure 3: A schematic demonstrating the scalar projection for an atom  $i$  (the reference atom) and one of its neighbor (1) along a direction  $\hat{u}$ . To generate the final fingerprint for atom  $i$ , a summation over the atoms within the cutoff sphere, as indicated by the dashed line, are considered.

To better understand the fingerprint described in Eq. ??, one can deconvolute it into three sub-



components (as separated by "."). The exponential term ( $e^{-\left(\frac{r_{ij}}{\eta}\right)^2}$ ) imposes a coordination shell around an atom  $i$  with  $\eta$  describes the extent of the shell. By using multiple such  $\eta$  values both nearby and distant coordination information are contained within the fingerprint. In this work,  $\eta$ 's were sampled on a logarithmic grid between  $[0.8\text{\AA}, 16\text{\AA}]$ , ensuring a sufficient description of the neighbor interactions. One could also use the peak positions of a radial distribution function as a starting point in choosing  $\eta$ 's. The normalized scalar projection ( $\frac{r_{ij}^u}{r_{ij}}$ ) adds directionality to the fingerprint by selectively resolving the coordination information along the desired direction, and is necessary to map the individual force components. Lastly, the damping function ( $f_d(r_{ij})$ ) diminishes the influence of far away atoms smoothly. The combination of these three features makes this particular choice of representation suitable for mapping atomic force components. Similar coordination based fingerprints have been developed in the past.<sup>14,27</sup> However, these were tailored for the purpose of mapping the total potential energy (a scalar quantity) for a given configuration of atoms, unlike the vectorial force components as done here.

Using Eq. ??, the fingerprint along the Cartesian directions for each atom within the database is computed (since the force components obtained from DFT are along these directions). However, one is not restricted to these 3 directions only. By creating a spherical mesh around an atom, several arbitrary directions ( $\hat{u}$  in Figure 3) can be defined for which we reconstruct the atomic force and recompute the fingerprint. Adding these quantities to the pre-existing reference database expands upon the wealth of atomic environments, with no additional *ab initio* calculations. Though such an undertaking further ensures diversity in the reference database it builds in extensive redundancies. Training a force field on millions of reference atomic environments is impractical, computationally very demanding, and might lead to misbehaved models, therefore, further down-sampling from within this big pool of data is an essential step in the construction workflow, and shall be discussed shortly.

## Properties of fingerprint

### Invariance

To demonstrate that the fingerprinting scheme proposed in Eq. ?? conforms to the basic invariance rules; translation, rotation and permutation of atoms, we refer the reader to Fig. 3. Each atom's position ( $\mathbf{r}_i$ ) is defined in the  $\mathbb{R}^3$ -Euclidean space, with atom  $i$  as the reference. A translation operation ( $\mathbf{t}$ ) on each atom shifts the position as  $\mathbf{r}'_i = \mathbf{r}_i + \mathbf{t}$ . However, given that Eq. ?? only considers pair-wise distances,  $r_{ij} = r'_{ij}$ , it does not alter the individual atomic fingerprint ( $V_i^u$ ). In the case of rotations a similar invariance property is observed. Consider rotating all neighboring atoms of  $i$  clock-wise, in Figure 3, about the z-axis by an angle  $\theta$  (for the subsequent discussion, we drop the index  $i$  for the atomic force components and fingerprint). Upon rotation both the force components and the corresponding fingerprints, along the Cartesian directions, change according to (shown here for forces but equally applicable for the fingerprint),

$$\begin{bmatrix} F^{x'} \\ F^{y'} \\ F^{z'} \end{bmatrix} = \begin{bmatrix} \cos(\theta) & -\sin(\theta) & 0 \\ \sin(\theta) & \cos(\theta) & 0 \\ 0 & 0 & 1 \end{bmatrix} \begin{bmatrix} F^x \\ F^y \\ F^z \end{bmatrix}.$$

Nevertheless, the net force before and after rotation are identical,  $F' = \sqrt{(F^{x'})^2 + (F^{y'})^2 + (F^{z'})^2} = F$ . As with the force components, the atomic fingerprints ( $V^u$ ,  $u \subset (x, y, z)$ ) change individually, but the net rotated quantity  $V' = \sqrt{(V^{x'})^2 + (V^{y'})^2 + (V^{z'})^2} = V$  is once again conserved, implying that the fingerprint transforms in a manner similar to the forces upon rotation. Lastly, permuting neighboring atoms only alters their indices, but given that the summand in Eq. ?? runs over all neighboring atoms within the cutoff sphere, the order of summation is unimportant and doesn't alter  $V_i^u$ .

## Uniqueness

Another important aspect of the fingerprint is that it remains unique for the diverse set of environments considered. The premise of AGNI, as mentioned earlier, is that the force is governed primarily by an atom's environment, as represented by its fingerprint. Numerically this implies that no two identical fingerprints should map to dissimilar forces. To identify the number of  $\eta$  values required to represent an atom, under which this hypothesis becomes true, we ask the question - *given an atom and its neighbors, can a different arrangement of the neighbors result in the same atomic fingerprint?* Consider two atomic arrangements,  $A$  and  $B$  with  $M$  and  $N$  atoms, respectively, with  $A$  being the reference. For a given  $\eta$  value, by freezing  $N - 1$  atom positions in  $B$ , the location of the free atom can be varied such that fingerprint is non-unique, though such an environment could be irrelevant. However, by using multiple  $\eta$  values, the probability of finding two high-dimensional identical fingerprints diminishes. In the limit that number of  $\eta$  values tends to  $\infty$  uniqueness can be ensured, nevertheless, for all practical purposes one can make do with a much smaller subset by running convergence tests.

## Clustering reference data

### Identifying redundancies

The next step in the construction workflow is selecting representative atomic environments for training purposes. To do so, it is necessary to identify the redundant and non-contributing data points from within the millions sampled. An obvious place to start is by comparing amongst the individual atomic fingerprints. However, given its high-dimensionality understanding or unraveling the fingerprint directly is non-trivial. Therefore, we rely on dimensionality reduction techniques such as principal component analysis (PCA) to project  $V_i^u$  onto a lower dimension space.<sup>28</sup> In PCA the original fingerprint is linearly transformed into uncorrelated and orthogonal pseudo variables, also known as principal components (PCs). This further permits visualization of the redundancies

present.

To demonstrate this, here, for all the reference atomic environments, we compute and transform an 8-dimensional fingerprint (the rationale for which shall be discussed shortly). Using the two relevant PCs (as majority of the variance,  $> 99\%$  is captured by them), the transformed fingerprints are visualized on this two-dimensional manifold, known as a scores plot (c.f., Figure 4). Immediately, we observe clustering of the different atomic environment types; for clarity environments corresponding to a few cases, e.g. adatoms, surfaces, vacancies, etc., are labeled. Further, by color coding atoms according to the dataset they were sampled from, i.e. A, B, C, D or E, we qualitatively observe their extent of diversity. For example, dataset D (c.f., Figure 4) spans a diverse set of atomic environments as it populates majority of the space, suggesting that isolated cluster configurations are a good starting point to sample reference data from. Interestingly, atomic environments from dataset E lie within the domain of dataset D. This suggests that a force field trained on dataset D should accurately predict the forces for environments in dataset E, though such configurations were never implicitly included in training.

## Selecting training and test data

The visualization tools described, thus far, provide a human-appealing method to identifying redundancies. To establish expedited and efficient force field construction an automated sampling of the PCA transformed data is necessary - to obtain the small but representative training dataset. One way of doing so is to choose the data randomly. Unfortunately, this biases sampling according to the underlying probability distribution of the dataset and fails to sample sparsely populated regions. To avoid such irregularities one could use k-means clustering methods to sparsify and identify a diverse set of atomic environments, as has been done in constructing machine learning force fields to predict total energies.<sup>29</sup> However, given the non-isotropic nature of our dataset k-means performs poorly. In this work, we adopt a simple grid-based sampling on the PCA space. Here, the PCA data is split into uniform sub-grids, the bounds of which are determined by the minimum and maximum of the relevant PCs. Training points are then randomly sampled from

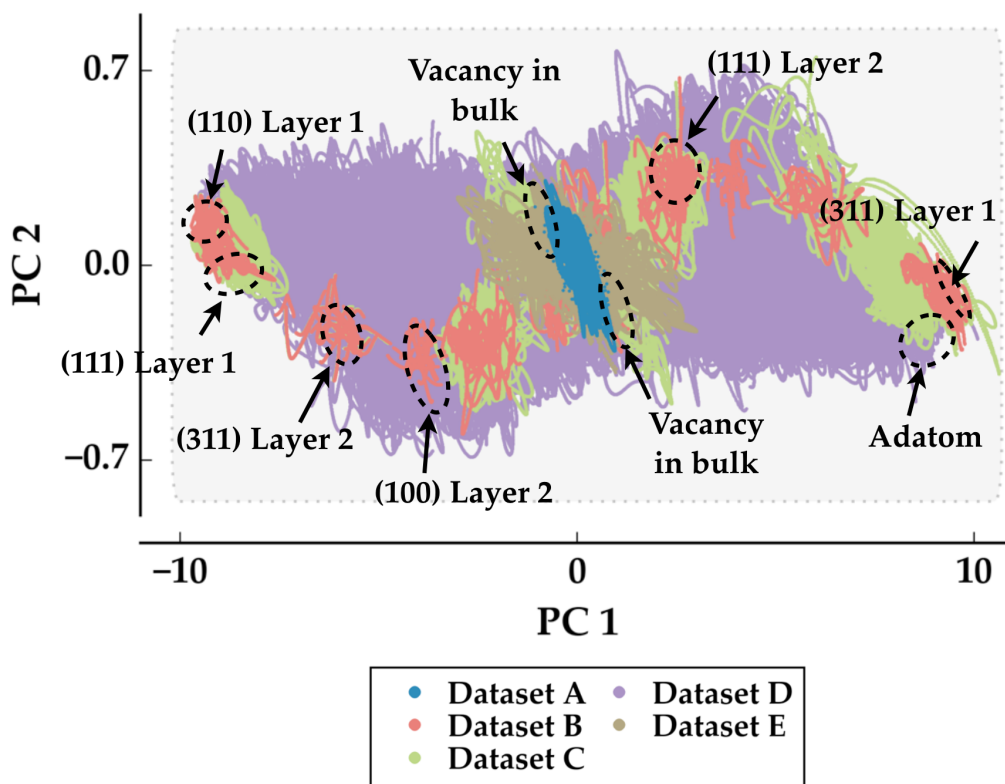


Figure 4: A projection of all the atomic fingerprints within dataset A, B, C, D, and E, onto a 2-dimensional manifold formed by the first two principal components. The original fingerprint was an 8 dimensional vector (i.e., 8 *eta* values) chosen to represent the environment around an atom.

within each sub-grid. By using a fine enough grid one can ensure uniform and diverse sampling from all regions of the PC space. Not that in the limit the grid size becomes large, the grid-based approach is equivalent to the random sampling approach. The validation test sets are generated in a similar manner from the remains of the non-sampled training data. Such clustering methods are critical as the learning and prediction cost scales as  $\mathcal{O}(n^3)$  and  $\mathcal{O}(n)$ , respectively (where  $n$  is the training dataset size).

## Learning algorithm

The next vital ingredient required in putting together a predictive framework is the learning algorithm itself. Deep learning neural networks<sup>30</sup> and non-linear regression processes<sup>15</sup> have been the methods of choice for models describing atomic interactions. Their capability to handle highly non-linear relations, as is in the case of mapping an atom’s environment to the force it experiences, makes them a suitable choice here as well. Here, we choose kernel ridge regression (KRR) as the machine learning workhorse.<sup>13,31</sup> KRR works on the principle of (dis)similarity, wherein, by comparing an atom’s fingerprint ( $V_i^u(\eta)$ ) with a set of reference cases, an interpolative prediction of the  $u^{\text{th}}$  component of the force ( $F_i^u$ ) can be made, and is given by

$$F_i^u = \sum_t^{N_t} \alpha_t \cdot \exp \left[ -\frac{(d_{i,t}^u)^2}{2l^2} \right]. \quad (2)$$

Here,  $t$  labels each reference atomic environment, and  $V_t^u(\eta)$  is its corresponding fingerprint.  $N_t$  is the total number of reference environments considered.  $d_{i,t}^u = \|V_i^u(\eta) - V_t^u(\eta)\|$ , is the Euclidean distance between the two atomic fingerprints, though other distance metrics can be used.  $\alpha_t$ s and  $l$  are the weight coefficients and length scale parameter, respectively. The optimal values for  $\alpha_t$ s and  $l$  are determined during the training phase, with the help of cross-validation and regularization methods. For further details concerning the learning algorithm the reader is directed to these sources.<sup>12,32,33</sup>

Finally, in order to evaluate the performance of a developed force field, three error metrics; mean absolute error (MAE), maximum absolute error (MAX), and the standard deviation (in particular  $2\sigma$ ), were chosen. Relying on multiple metrics reduces any bias, unknowingly, introduced during model selection as shall be discussed shortly.

## Uncertainty quantification

The final component to a successful predictive model is to be able to quantify uncertainty in the predictions made. For instance, *given a force field can we estimate the prediction error on the atomic forces for a new observation?* Finding solutions to such questions, will help enable one to understand the domain of applicability of their respective models. As with any statistical model, the true value of the force ( $F^*$ ) for a given atom can be expressed as the predicted value ( $F$ ) with some error ( $\varepsilon$ ), given as

$$F^* = F + \varepsilon. \quad (3)$$

If  $\varepsilon$  can be statistically estimated we then have a pathway to provide confidence bounds on the predicted atomic force.

In the KRR framework, for every new observation the distance,  $d_t$  (for brevity we only label the reference environment and dropped the observation and direction label,  $i$  and  $u$ , respectively), between its fingerprint and the reference training fingerprints is computed (resulting in a total of  $N_t$  distances). The final prediction is then a weighted sum of the list of distances, making these distances an important metric on predictive accuracy. Amongst the list of distances, the minimum distance,  $d_{min} = \min\{d_1, d_2, \dots, d_{N_t}\}$ , in particular provides a measure of *closeness* of the new observation to the training cases, and can be thought of as a descriptor in estimating  $\varepsilon$ . To capture the correlation between  $d_{min}$  and  $\varepsilon$ , for every observation in the test dataset we compute  $d_{min}$  and  $\varepsilon (= F^* - F)$ . By binning the range of  $d_{min}$ s observed into uniform and smaller sub-groups, a standard normal distribution function is fit to the observed  $\varepsilon$ . For each sub-group, collecting

standard deviation ( $s$ ) statistics of the normal distribution, ultimately, provides an estimate of  $\epsilon$  as a function of  $d_{min}$  (with a confidence level of 68.2%, though higher confidence levels can be equally implemented).

## Constructing the force field

At this stage all the pieces required to construct AGNI force fields, as illustrated by the flowchart in Figure 1, have been laid out. In the upcoming sections we discuss how one chooses the appropriate number of  $\eta$  values describing an atomic environment, or the size of training data to use. These are important parameters that one needs to thoroughly test to ensure accurate force fields. The accepted force field is then put to test by predicting forces on atoms outside the domain of training environments used, to ensure its generalizability. Lastly, a distance based model to estimate uncertainty in force prediction is provided.

## Convergence tests

The first step to attaining an optimal force field is to ensure convergence with respect two parameters: (i) the number of  $\eta$  values used for the atomic fingerprint, and (ii) the training dataset size. As mentioned earlier the number of  $\eta$  values governs the resolution with which an atom’s local coordination environment is described, while, the size (and choice, as shall be elaborated in the next section) of training data governs AGNI’s interpolative predictive capability. In order to identify this optimal parameter set, we systematically increase the fingerprint resolution from 2 to 16  $\eta$  values and the training dataset size from 100 to 2000 atomic environments, while monitoring test set error (in this case the chosen error metric was the MAE). To remind the reader,  $\eta$  values were sampled on a logarithmic grid between  $[0.8\text{\AA}, 16\text{\AA}]$ , while training data environments were sampled using the PCA projection followed by a grid-based sampling.

For each of the four training datasets (A, B, C and D), partitioned in the data generation stage, and for all combinations of the convergence parameters an AGNI force field was constructed.



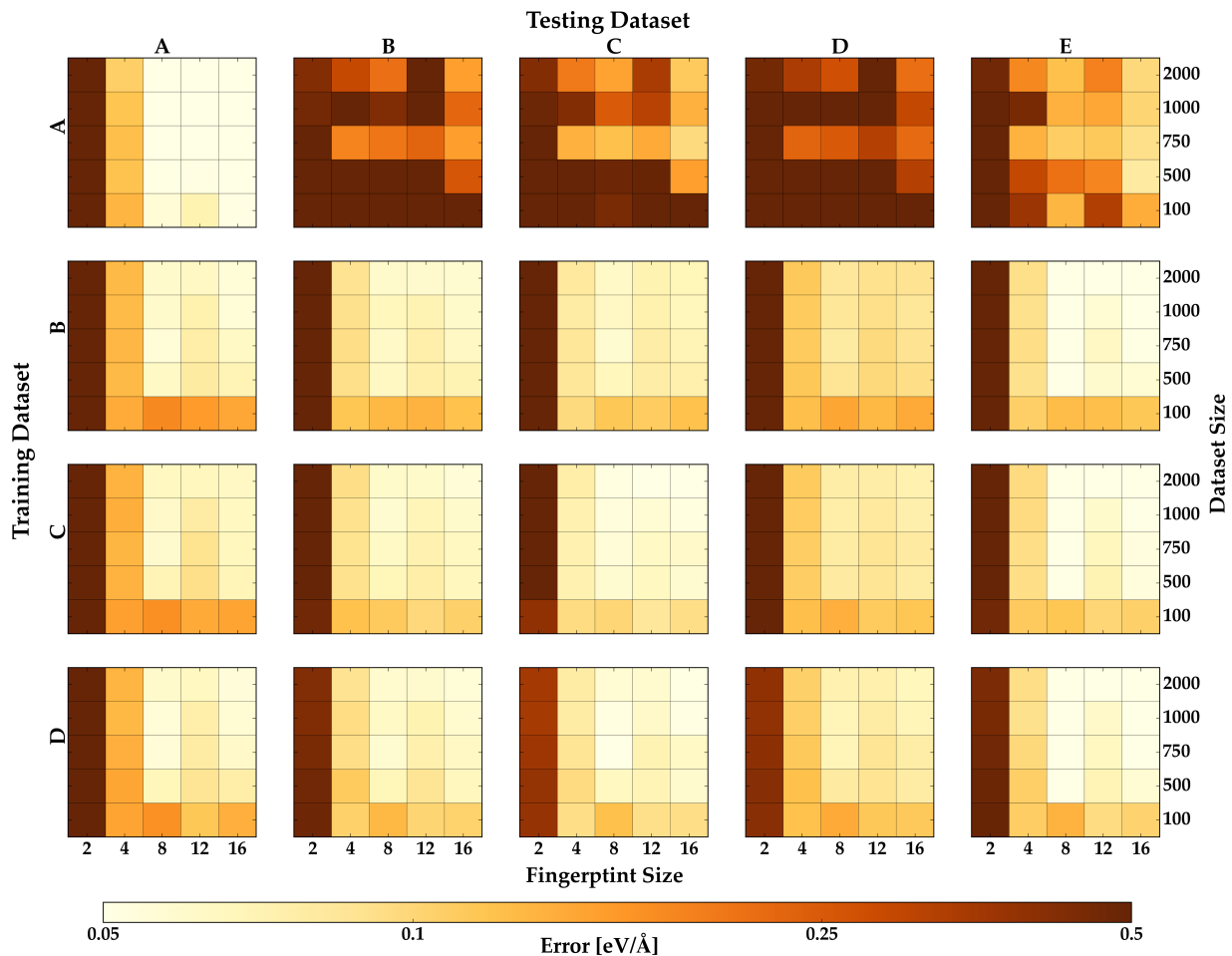


Figure 5: Heat maps illustrating model error (mean absolute error) as a function of number of  $\eta$  values and the training dataset size. The fingerprint was varied from 2 to 16  $\eta$  values, while the training dataset size was varied from 100 to 2000 environments. We report the MAE for models trained on datasets A, B, C, and D and tested on datasets A, B, C, D, and E. For example the top row corresponds to models trained on dataset A, while each column corresponds to a test datasets of the five cases. The errors quickly converge for a fingerprint with 8  $\eta$  values and a training size of 1000 diverse environments.

Each force field is then validated on the respective test datasets (A, B, C, D and E). The force fields are denoted as  $M_i^j$ , where  $i$  and  $j$  label the training and test environments used, respectively (the superscript is omitted when referring to the training environments only). Figure 5 illustrates heat maps of the error for different training and test datasets, and convergence parameter combinations. Two key findings stand out: (i) by increasing the fingerprint resolution the error drops and quickly converges below  $\approx 0.05$  eV/Å (expected chemical accuracy), and (ii) increasing the training dataset size reduces error only beyond a reasonable fingerprint resolution. For example, in  $M_C^A$  increasing the training dataset size for a fingerprint with 2 or 4  $\eta$  values has no effect on the predictive capability. Such a manifestation implies that 8 or more  $\eta$  values are required to “uniquely” discern amongst the atomic environments, in order for the learning algorithm to work. Nevertheless, this relation only holds for force fields used in an interpolative manner, as seen in the failure of  $M_A^B$ ,  $M_A^C$ ,  $M_A^D$  or  $M_A^E$ . Here, the diversity in the training data chosen plays a more prominent role in governing performance, as shall be elaborated in the next section. Overall, we find that a fingerprint of 8  $\eta$  values and a training size of 1000 atomic environments is sufficient, beyond which the models exhibit diminishing returns, i.e. increased model training costs with no significant drop in model error, and are the parameters chosen for all subsequent discussions. The computational burden of each AGNI prediction is  $\approx 0.1$ ms/atom/core, while DFT costs  $\approx 1$ ks/atom/core.

## Training data choice

The particular choice of atomic environments included during training is a crucial factor, as briefly alluded to earlier. Given that the learning algorithm is interpolative by nature, a force field trained say only on bulk type environments ( $M_A$ ) cannot predict the forces corresponding to other environments types, e.g. datasets with surfaces and other features -  $M_A^B$ ,  $M_A^C$ ,  $M_A^D$  or  $M_A^E$ . By increasing the diversity in training environments,  $M_B$ ,  $M_C$  and  $M_D$ , we make the force fields more generalizable once the optimal parameters are chosen, as given by their low test error in Figure 5. Surprisingly, it appears as though predictions made with  $M_B$  are equally as good as  $M_C$  or  $M_D$ . However, this is purely a manifestation of using the MAE as the error metric. Along with the MAE, we report

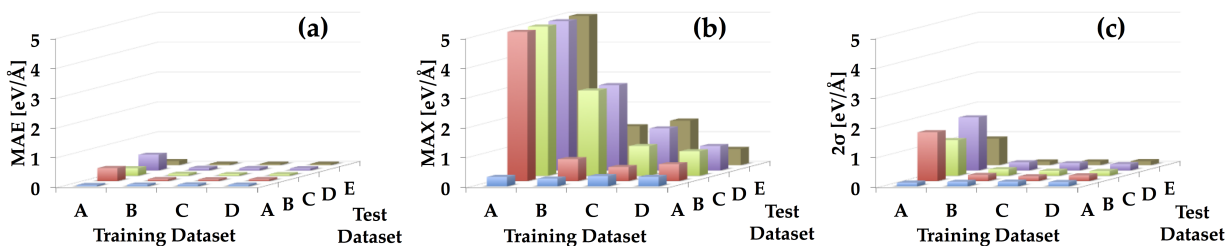


Figure 6: (a) Mean absolute error, (b) maximum absolute error, and (c)  $2 \cdot$  standard deviation error metric, for models trained on A, B, C and D and tested on dataset A, B, C, D and E. The errors are reported for an 8 dimensional fingerprint vector (i.e., 8 *eta* values) chosen to represent the environment around an atom, and a training set size of 1000 environments obtained from the PCA grid-based sampling.

test set errors computed with two other metrics - MAX and  $2\sigma$ , as illustrated in Figure 6 (shown only for the optimal 8-component fingerprint and 1000 training atomic environments). For  $M_B$ , with MAX as the metric, the prediction error is high outside its domain of applicability (test set C, D or E), and a similar behavior is observed for  $M_C$ . It should be recognized that MAX reports the worst prediction made, while MAE reports a mean error skewed by test set size. By combining the two metrics with the actual variance in the errors, as measured by the  $2\sigma$  metric, we can ensure that the error is indeed under control. We observe that in  $M_D$ , by sampling atomic environments from a very diverse set of configurations all the error metrics are low, and the force field is highly generalizable, and is the force field used in subsequent discussions.

## Testing out of domain configurations

The configurations contained in dataset E; grain boundaries, lattice expansion and compression, and dislocations, were never “observed” during the training phase. Being able to accurately predict the forces will further demonstrate the fidelity in using local-neighborhood based AGNI force fields. The PCA scores plot, shown in Figure 4, provided a glimpse of what one could expect. Given that the transformed atomic fingerprints for dataset E lies within the domain of environments from dataset D, it qualitatively confirms that predictions made by  $M_D$  are interpolative and thus should be accurate. However, a more stringent test is to predict forces on all the atoms in

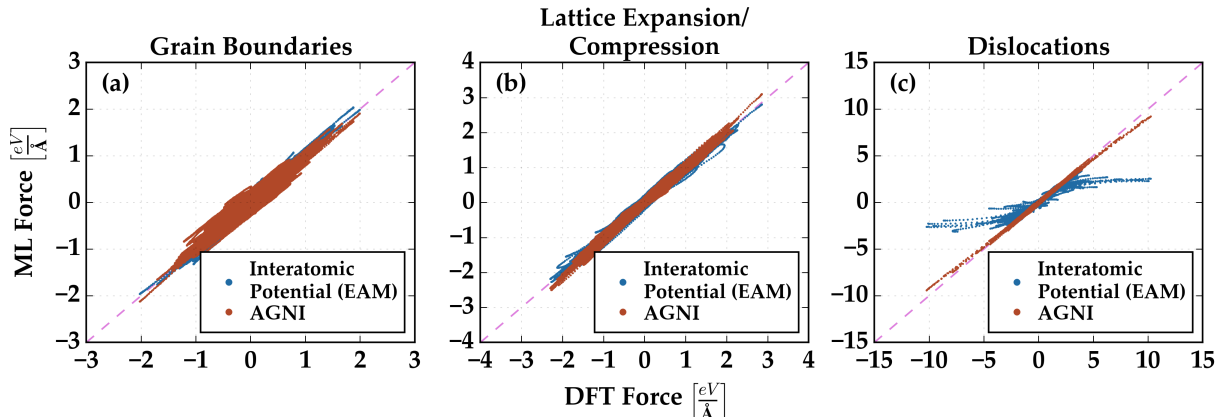


Figure 7: Parity plots comparing force predictions, for test environments in dataset E, made with the AGNI model,  $M_D$ , EAM interatomic potential, and DFT. The plots have been further separated according to the configuration they were sampled from, (a) grain boundaries, (b) lattice expansion/compression, and (c) dislocation, respectively.

dataset E and compare them to those obtained by DFT methods. As is done and shown in Figure 7. For all three cases, the AGNI predicted forces are in excellent agreement with DFT. This demonstrates, for the first time, the intended goal of AGNI force fields, i.e. to retain quantum mechanical accuracy, be computationally inexpensive, and remain generalizable. The last feature in particular, generalizability, is often lacking with traditional semi-empirical methods. For comparison, we recompute the forces for the atoms in dataset E using traditional semi-empirical potentials. Here, we particularly use an Al EAM potential,<sup>34</sup> as it accurately captures interactions in close-packed metallic type systems. As with AGNI force field, EAM methods equally predict forces accurately for grain boundaries and lattice expansion/compression but fails for dislocation type of environments. This once again raises an important question in the realm of force field based simulations - *can one a priori judge the error in the forces predicted?* In the next section we provide one such attempt at estimating uncertainties in the force predictions made with AGNI.

## Quantifying the uncertainty

Quantifying uncertainties is a challenging task that can at best be done probabilistically. Here, using such a framework laid out earlier, we discuss how one can generate uncertainty estimates

for force predictions. Using  $M_D$  as the force field, for each test environment (in dataset A, B, C, D and E) we compute  $\varepsilon$  of the predicted force, as given in Eq. ??, and the corresponding  $d_{min}$ , i.e. minimum distance within the training dataset. The results are summarized in the scatter plot of Figure 8. Clearly, as  $d_{min}$  increases, the variance within  $\varepsilon$  rises for a particular choice of  $d_{min}$ . Upon binning the data into smaller sub-groups as indicated by the dashed lines, a standard normal distribution function is fit. The histogram insets in Figure 8 demonstrate this for three such bins.  $d_{min} < 10^{-3}$  were ignored as the data was too sparse for statistical interpretation. While, a cutoff  $d_{min} > 10^{-1}$  was imposed, beyond which the variance in the force predictions is too high. These regions are indicated by the gray-filled rectangles in Figure 8. Access to the standard deviation ( $s$ ) for each bin, allows us to provide a confidence estimate for the predictions made as a function of  $d_{min}$ . Upon plotting  $d_{min}$  and  $s$  for all the bins (red circle markers), as shown in Figure 9, we observe a trend, wherein, as  $d_{min}$  increases the uncertainty in the predicted force increases. At low  $d_{min}$ , a polynomial behavior with  $s$  is observed ( $s = 49.1d_{min}^2 - 0.9d_{min} + 0.05$ , as shown by the dashed blue line in Figure 9).

The proposed polynomial relation serves as a rudimentary estimate to the upper bound of prediction error. The relation in Figure 9 is symbolic of a typical interpolative model, whereby, if training data exists in the vicinity of a new observation confident predictions can be made. It is for these reasons; we employ diversification and filtering techniques to ensure that the model spans a diverse environment space uniformly in order to make reasonably accurate predictions. By quantifying uncertainty, it allows one to identify those atomic environments likely to result in high prediction errors. By flagging and accumulating such environments one can systematically retrain the force fields, resulting in an adaptive refinement of accuracy and generalizability over time.

## Validating the force field

Having demonstrated a robust scheme that allows accurate atomic force predictions for a diverse set of situations, in the subsequent sections, we demonstrate the true prowess of such AGNI force

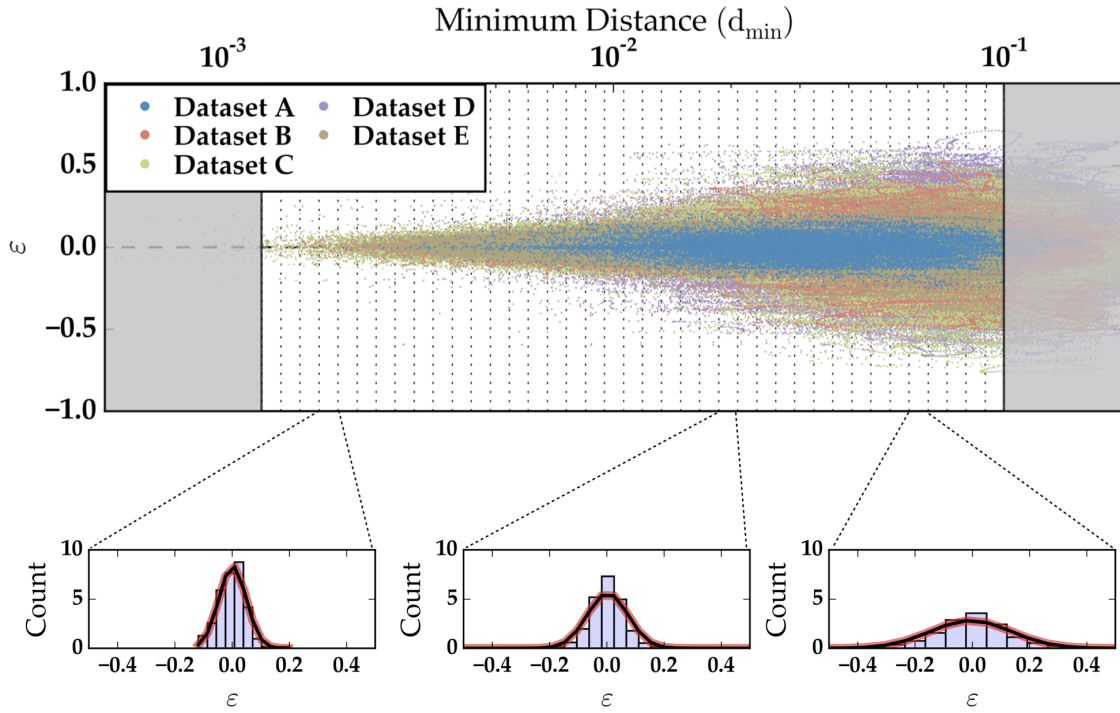


Figure 8: Top panel: a scatter plot of the minimum distance ( $d_{min}$ ) vs. the predicted force error ( $\epsilon$ ). The range of  $d_{min}$  is further sub-divided into small groups for statistical analysis. The gray regions were not considered for any statistical purposes, due to the lack of sufficient data (left) and high errors (right). Bottom panel: a standard normal distribution fit for each sub-group (though only shown for three such bins), used to estimate the variance in model errors.

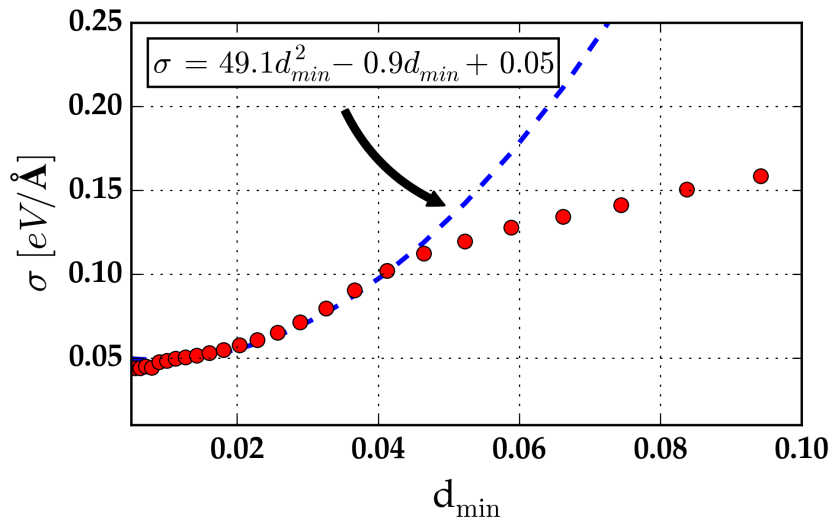


Figure 9: The uncertainty model, created for force field  $M_D$ , whereby  $d_{min}$  is used as a descriptor to measure the expected variance in the prediction made. The markers show the actual behavior, while the blue dashed line indicates a polynomial fit to the uncertainty.

fields in facilitating atomistic simulations. Our previous work provided a glimpse of such simulations, whereby, structural optimization, vibrational property estimation, as well as simple MD simulations were undertaken.<sup>18</sup> Here, we extend the realm of such force fields to simulate complex atomistic phenomena, such as melting and stress-strain behavior. These are particularly challenging as the atoms traverse through a multitude of environments, and an accurate prediction of the forces requires undertaking the rigorous construction workflow discussed thus far.

The simulations were carried out using the LAMMPS molecular dynamics code.<sup>35</sup> The source code and force field files required to carry out the simulations are provided as supplemental files.

### Melting behavior of an Al (111) surface

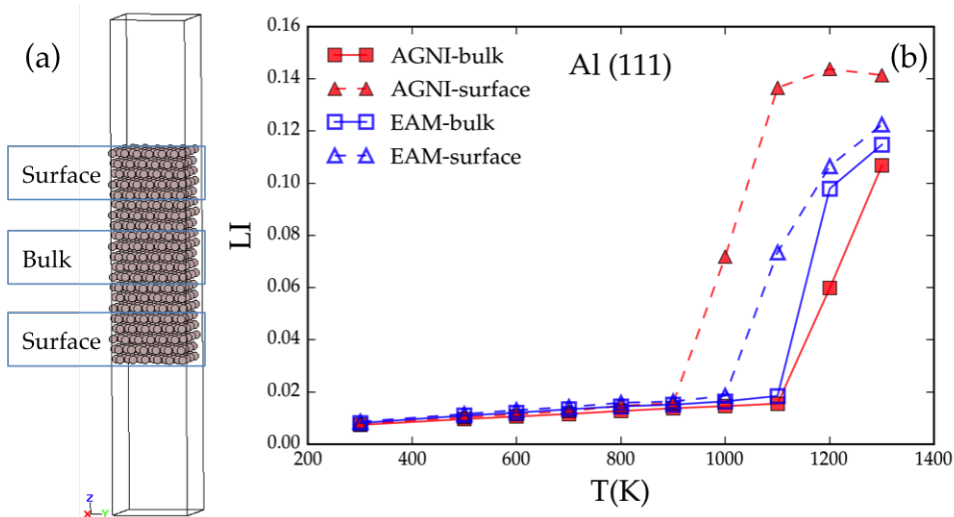


Figure 10: (a) A schematic of the (111) Al surface model and the regions classified as surface or bulk atoms. (b) The Lindemann index (LI) as function of temperature simulated with both the AGNI and EAM force fields. Melting occurs once the LI transitions from a slow linear increase to a sudden spike. With the AGNI force field the surface begins to melt  $\sim 950$  K, and propagates to the bulk by  $\sim 1100$  K.

The melting temperature of condensed matter is a property often estimated by MD simulations. Here, starting with a surface model with over 1000 atoms and dimensions of  $19 \times 17 \text{ \AA}$  (c.f., Figure 10(a)), constant temperature MD simulations were carried out for over 50 ps and across a temperature range of 300 - 1300 K, to estimate the melting temperature. In traditional MD

simulations, energy is used as the metric to distinguish between a melt and non-melt state, and since this metric is not at our disposal we rely on a structural order parameter instead. In particular, we rely on the Lindemann Index (LI) as it has been shown that a first order transition in the LI can be attributed to the melting transformation.<sup>36-38</sup> The LI is defined as,

$$LI = \frac{1}{N} \sum_i \frac{1}{N-1} \sum_{j \neq i} \frac{\sqrt{\langle r_{ij}^2 \rangle - \langle r_{ij} \rangle^2}}{\langle r_{ij} \rangle} \quad (4)$$

where  $r_{ij}$  is the distance between atom  $i$  and  $j$ ,  $N$  is the total number of atoms, and  $\langle \dots \rangle$  indicate time averaged quantities.<sup>39</sup> For the range of temperatures considered the LI was computed using Eq. ?? and reported in Figure 10(b) (red lines). Further, we distinguish between the surface and bulk LI values (c.f., 10(a)) as it is well known that the melt front initiates at the surface and propagates inwards. Starting at 300 K, the LI rises due to a systematic increase in thermal vibrations up to 900 K. Between 900 - 1000 K, the sudden increase in LI signifies the transition into a melt state at the surface, which then propagates into the bulk by 1200 K. With AGNI force fields an onset of melting observed at  $\sim 950$  K, similar to the known experimental value at  $\sim 933$  K for Al.<sup>40</sup> Even though the training environments used in building  $M_D$  did not explicitly contain Al in a liquid state, by including high temperature MD reference data we were able to predict forces for environments in such extreme conditions. Similar LI curves computed by an EAM force field, as pure *ab initio* studies of this size and timescale are intractable, yielded an overestimated melting temperature of  $\sim 1100$  K.

## Stress-strain behavior of an Al (001) surface

Another important material property determined by atomistic simulations is the stress-strain behavior. Beginning with a (001) fcc Al surface, of dimensions  $8 \times 8 \times 80$  Å, the surface atoms (fixed in their position) are displaced,  $\Delta l$ , resulting in a uniaxial strain along the surface normal [001] as illustrated in Figure 11(a). Atoms within the strained region are then relaxed to minimize the forces acting upon them. This imposes a net force ( $F_s$ ) on the fixed surface atoms towards the



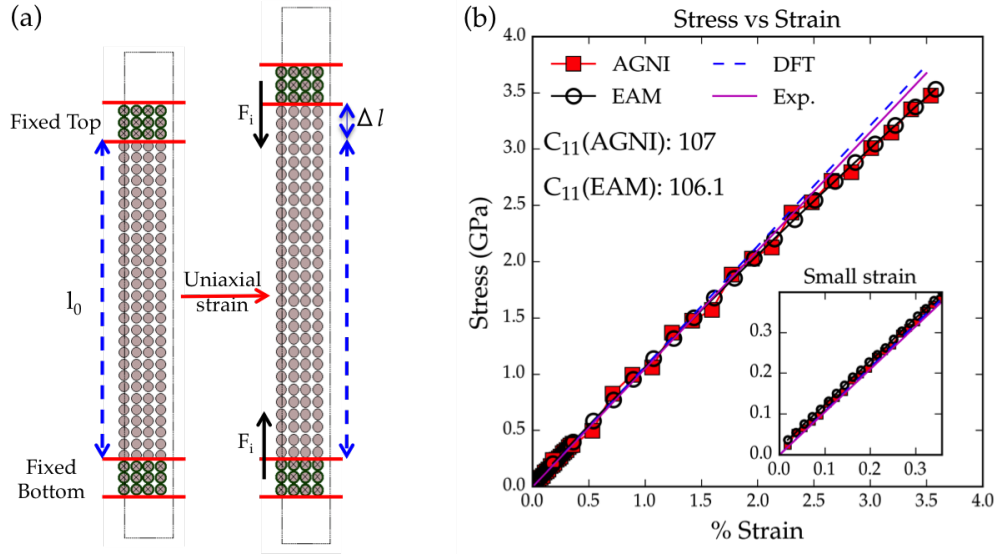


Figure 11: (a) A schematic of the surface model and procedure adopted to extract stress-strain behavior. (b) Stress vs. strain behavior of uni-axially strained Al as computed using forces predicted by the AGNI and an EAM force field. The inset shows stress at low strain ( $< 0.35\%$ ).

bulk (c.f., Figure 11(a)). Using the stress tensor relation,  $\sigma_{s,p} = \frac{F_s}{A_p}$ , for a plane  $p$  with an area  $A_p$ , across varying values of strain,  $\varepsilon_{s,p} = \frac{\Delta l}{l_0}$ , one can deduce the stress-strain behavior of the material. In Figure 11(b) we report the computed stress for varying strain deformations. The slope of this curve, for the direction considered, yields the  $C_{11}$  elastic coefficient, a property that can be compared with atomistic theories. Using the AGNI force field we report a  $C_{11}$  value of 107 GPa, which is in good agreement with a past *ab initio* result of 105 GPa.<sup>41</sup> Clearly, this suggests that besides forces the force field can predict their derivatives, i.e., the stresses, at quantum mechanical accuracy as well. Further, we recomputed the  $C_{11}$  value with an EAM potential, resulting in a value of 106 GPa. Though, the combination of AGNI force prediction and stress relation result in quantum mechanically accurate elastic coefficients, the procedure laid out can only describe the stress along non-periodical directions, a limitation of the force based implementation.

## Energy prediction

We now briefly touch upon the topic of energy. Energy is a unique, and important, global quantity describing the state of a configuration of atoms. It is often used to ensure stable MD simulations,

estimate phase diagrams, compute minimum energy reaction pathways, etc. Given the principium of AGNI, whereby, the force on an atom is learnt based on its environment deprives the means to predicting energy directly. Nevertheless, we now discuss some alternative strategies to estimating energy, be it in dynamic or static simulations.

### During a molecular dynamics simulation

The rate of change of the total potential energy, in an MD simulation, can be expressed as a function of the individual atomic forces and velocities by invoking the chain rule,

$$\frac{dE}{dt} = \sum_{i,u} \frac{\partial E}{\partial r_i^u} \frac{\partial r_i^u}{\partial t} = - \sum_{i,u} F_i^u v_i^u. \quad (5)$$

$E$  is the total potential energy of the system,  $r_i^u$  and  $v_i^u$  are the position and velocity of atom  $i$  along one of the three coordinates,  $u \in (x, y, z)$ . By choosing a small time differential in Eq. ??, which corresponds to a small time step ( $\Delta t$ ) in the MD simulation, an expression for the energy can be derived as,

$$E_t = E_{t-\Delta t} - \Delta t \left( \sum_{i,u} F_i^u v_i^u \right). \quad (6)$$

The above expression provides a pathway to monitor the energy during the course of a MD simulation, in reference to that of the initial configuration. To validate this scheme, constant temperature MD simulations of bulk fcc Al were carried out at different temperatures using the  $M_D$  AGNI force field, and the corresponding AGNI predicted energies were computed using Eq. ?. In each simulation a  $\sim 250$  atom cell and a time step of 0.5 fs were used. For comparison, DFT energies were computed for a few configurations generated from different temperature MD trajectories. In each case the energy of perfect fcc Al was set to zero. The energies computed by both these methods are plotted in Figure 12(a). Clearly, the predicted energy is conserved in time, while maintaining the correct ordering with temperature. The root mean square error between the predicted and the DFT energy is  $\approx 4$  meV/atom, on the order of numerical noise. Similar energy predictions made by an EAM force field (Figure 12(b)) displayed similar trends.

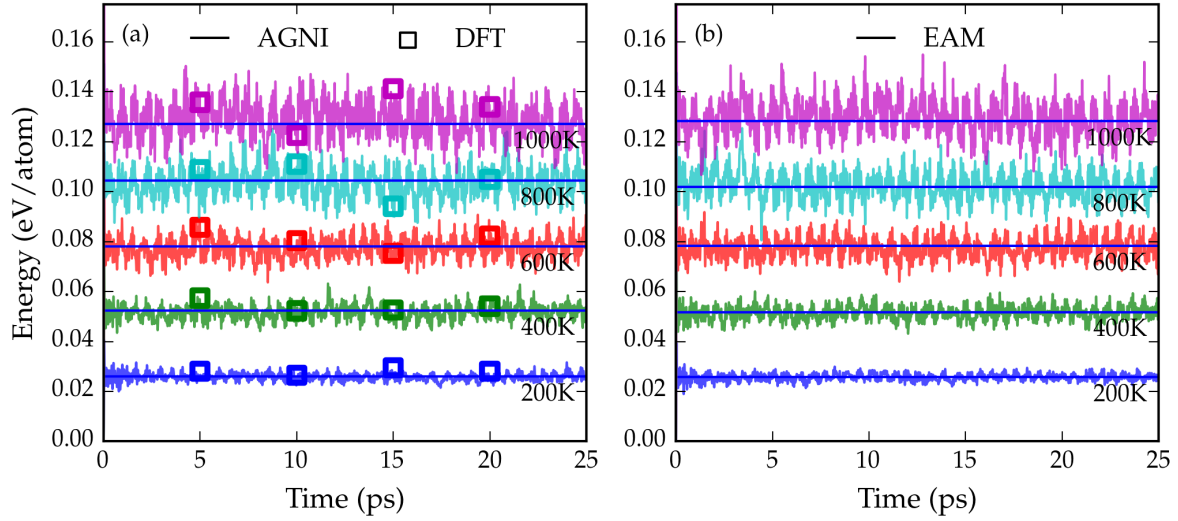


Figure 12: Evolution of energy of bulk fcc Al using the (a) AGNI with Eq. ??, and (b) EAM potential. DFT computed energies of a few configurations are also marked in (a) for validation. In all the cases, the energy is in reference to that of the perfect fcc Al. The energy is conserved with time and maintains the correct ordering with temperature.

### During a static simulation

A second, and equally simple, approach to estimating the potential energy directly from forces is by integrating them using a Taylor series approximation of the potential energy

$$\begin{aligned}
 E &= E_o + \sum_{i,u} \left( \left. \frac{dE}{dr_i^u} \right|_{r_i^u=r_o} (r_i^u - r_o) + \frac{1}{2!} \left. \frac{d^2E}{dr_i^{u2}} \right|_{r_i^u=r_o} (r_i^u - r_o)^2 + \dots \right) \\
 &\cong E_o - \sum_{i,u} F_i^u \Delta r_i^u, u \subset (x,y,z)
 \end{aligned} \tag{7}$$

Here,  $E$  is once again the total potential energy, which to a first order approximation can be derived from the atomic forces.  $r_i^u$  is once again the atomic position. A discretization along the atomic positions governs the accuracy by which we can predict the energy. For these reasons Eq. ?? is particularly more suited for static simulations, e.g. computing reaction barriers along a reaction coordinate, when the velocities are zero. The validity of this approach was demonstrated to be consistent with the underlying potential energy surface in our previous work, whereby, the migration energy for a vacancy in bulk Al was within 3% of the DFT predicted value.<sup>18</sup>

Eqs. ?? and ?? both provide a restricted means to computing the energy, whereby, it is necessary that a pathway connecting the different configurations in phase space (either in time or along a reaction coordinate) exists, in order to accurately carry out force integration. This is a limitation of using a truly force based force field, wherein, one cannot predict energies by simply choosing two arbitrary points in the phase space. Nevertheless, these findings ascertain that Eq. ?? and ?? can indeed be used to compute change in the total potential energy as a function of time or reaction coordinate, as needed by a majority of atomistic simulations.

## Outlook and Summary

A new machine learning framework to circumvent the accuracy, cost, and generalizability issues facing current atomistic models has been proposed. By directly mapping quantum mechanical derived force components to the numerical representation of an atom's local environment, accurate and computationally inexpensive force fields, herein called AGNI, were developed. In this manuscript a workflow for their systematic construction, which includes generating reference data, representing the atomic environments with a numerical fingerprint, sampling non-redundant data, learning the forces, were all demonstrated for the example of elemental Al. Further, methods to quantify uncertainties in the force predictions are proposed. This is crucial to understand the domain of applicability of such data-driven force fields, in turn paving the way for their adaptive refinement.

Nevertheless, to make such methods a mainstream tool for atomistic simulations a few challenges yet remain that need to be addressed. Firstly, to explore diverse chemistries it is necessary to come up with AGNI force fields for multi-elemental systems in an equally quick and rational manner. Though the framework discussed here was for an elemental system, the recipe is directly transferable to multi-elemental situations. Secondly, as materials science or chemical systems become ever increasingly complex, the configuration space to be explored will increase exponentially. This poses a challenge for the non-linear regression learning algorithm proposed here, and

for a continued realization of machine learning force fields adopting methodologies, wherein, large quantities of data can be handled will be required.

Irrespective of these challenges, the prospect of using AGNI force fields as a tool to accelerate atomistic simulations is indeed very promising. Access to such high fidelity force predictions at a fraction of the cost has already made significant inroads to studying materials and chemical phenomena. Our previous work demonstrated an expose of some atomistic simulations, such as; geometry optimization of atomic structures with several 100s of atoms, dynamical evolution of defects over long time scales (vacancies and adatoms) to determine diffusion barriers, computing vibrational properties of materials, and estimating reaction energy barriers, all using AGNI force fields.<sup>18</sup> Here, we further extended the scope of such force fields by simulating even more complex phenomena - estimating the melting and stress-strain behavior of Al surfaces. Also, methods to predict energies entirely from forces were proposed. The force field construction workflow put in place here allowed us to study these more complex materials and chemical phenomena, and such strategies are only going to become increasingly important in pushing the envelope of atomistic simulations.

## Acknowledgment

This work was supported financially by the Office of Naval Research (Grant No. N00014-14-1-0098). The authors would like to acknowledge helpful discussions with K. B. Lipkowitz, G. Pili- nia, T. D. Huan, and A. Mannodi-Kanakkithodi. Partial computational support through a Extreme Science and Engineering Discovery Environment (XSEDE) allocation is also acknowledged.

## References

- (1) Tadmor, E. B.; Miller, R. E. *Modeling Materials: Continuum, Atomistic and Multiscale Tech- niques*; Cambridge University Press, 2012; pp 153–300.
- (2) Hautier, G.; Jain, A.; Ong, S. P. *J. Mater. Sci.* **2012**, *47*, 7317–7340.

- (3) Becke, A. D. *J. Chem. Phys.* **2014**, *140*.
- (4) Burke, K. *J. Chem. Phys.* **2012**, *136*, 150901.
- (5) Bickelhaupt, F. M.; Baerends, E. J. *Reviews in Computational Chemistry*; John Wiley and Sons, Inc., 2007; pp 1–86.
- (6) Neugebauer, J.; Hickel, T. *Comp. Mol. Sci.* **2013**, *3*, 438–448.
- (7) Hill, J.-R.; Freeman, C. M.; Subramanian, L. *Use of Force Fields in Materials Modeling*; John Wiley and Sons, Inc., 2007; pp 141–216.
- (8) Torrens, I. M. *Interatomic potentials*; Academic Press Inc., 1972.
- (9) Elliott, J. A. *Int. Mat. Rev.* **2011**, *56*, 207.
- (10) Bianchini, F.; Kermode, J. R.; Vita, A. D. *Modelling and Simulation in Materials Science and Engineering* **2016**, *24*, 045012.
- (11) Witten, I. H.; Frank, E.; Hall, M. A. *Data mining: Practical machine learning tools and techniques*; Elsevier, 2011.
- (12) Hastie, T.; Tibshirani, R.; Friedman, J. *The Elements of Statistical Learning: Data Mining, Inference, and Prediction*, 2nd ed.; Springer: New York, 2009.
- (13) Hofmann, T.; Scholkopf, B.; Smola, A. J. *Ann. Statist.* **2008**, *36*, 1171.
- (14) Behler, J. *J. Chem. Phys.* **2011**, *134*, 074106.
- (15) Bartók, A. P.; Payne, M. C.; Kondor, R.; Csányi, G. *Phys. Rev. Lett.* **2010**, *104*, 136403.
- (16) Lorenz, S.; Groß, A.; Scheffler, M. *Chem. Phys. Lett.* **2004**, *395*, 210 – 215.
- (17) Botu, V.; Ramprasad, R. *Int. J. Quant. Chem.* **2015**, *115*, 1074–1083.
- (18) Botu, V.; Ramprasad, R. *Phys. Rev. B* **2015**, *92*, 094306.

- (19) Li, Z.; Kermode, J. R.; De Vita, A. *Phys. Rev. Lett.* **2015**, *114*, 096405.
- (20) Kohn, W.; Sham, L. J. *Phys. Rev.* **1965**, *140*, A1133–A1138.
- (21) Hohenberg, P.; Kohn, W. *Phys. Rev.* **1964**, *136*, B864–B871.
- (22) Car, R.; Parrinello, M. *Phys. Rev. Lett.* **1985**, *55*, 2471–2474.
- (23) Kresse, G.; Furthmüller, J. *Phys. Rev. B* **1996**, *54*, 11169.
- (24) Kresse, G.; Joubert, D. *Phys. Rev. B* **1999**, *59*, 1758.
- (25) Perdew, J. P.; Burke, K.; Wang, Y. *Phys. Rev. B* **1996**, *54*, 16533.
- (26) Blöchl, P. E. *Phys. Rev. B* **1994**, *50*, 17953.
- (27) Bartók, A. P.; Kondor, R.; Csányi, G. *Phys. Rev. B* **2013**, *87*, 184115.
- (28) Jolliffe, I. *Statistics Reference Online*; John Wiley and Sons, Inc., 2014.
- (29) Szlachta, W. J.; Bartók, A. P.; Csányi, G. *Phys. Rev. B* **2014**, *90*, 104108.
- (30) Behler, J. *Phys. Chem. Chem. Phys.* **2011**, *13*, 17930.
- (31) Müller, K. R.; Mika, S.; Ratsch, G.; Tsuda, K.; Scholkopf, B. *IEEE Trans. Neural Networks* **2001**, *12*, 181.
- (32) Hansen, K.; Montavon, G.; Biegler, F.; Fazil, S.; Rupp, M.; Scheffler, M.; von Lilienfeld, O. A.; Tkatchenko, A.; Müller, K. *J. Chem. Theory Comput.* **2013**, *9*, 3404.
- (33) Rupp, M. *Int. J. Quant. Chem.* **2015**, *115*, 1058–1073.
- (34) Jacobsen, K. W.; Norskov, J. K.; Puska, M. J. *Phys. Rev. B* **1987**, *35*, 7423–7442.
- (35) Plimpton, S. *Journal of computational physics* **1995**, *117*, 1–19.
- (36) Alavi, S.; Thompson, D. L. *J. Phys. Chem. A* **2006**, *110*, 1518–1523, PMID: 16435812.

- (37) Neyts, E. C.; Bogaerts, A. *J. Phys. Chem. C* **2009**, *113*, 2771–2776.
- (38) Zhang, K.; Stocks, G. M.; Zhong, J. *Nanotechnology* **2007**, *18*, 285703.
- (39) Zhou, Y.; Karplus, M.; Ball, K. D.; Berry, R. S. *J. Chem. Phys.* **2002**, *116*, 2323–2329.
- (40) Stoltze, P.; Nørskov, J. K.; Landman, U. *Phys. Rev. Lett.* **1988**, *61*, 440–443.
- (41) Pham, H. H.; Williams, M. E.; Mahaffey, P.; Radovic, M.; Arroyave, R.; Cagin, T. *Phys. Rev. B* **2011**, *84*, 064101.